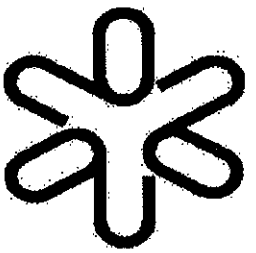

# Instituto de Física
# Universidade de São Paulo

**Droplet formation in cold asymmetric nuclear matter in the quark-meson-coupling model**

Krein, G.

*Department of Physics , University of Washington, USA*

Menezes, D. P.

*Instituto de Física - CFM, Universidade Federal de Santa Catarina, Florianópolis, SC, Brasil*

Nielsen, M.

*Instituto de Física, Universidade de São Paulo, SP, Brasil*

Providência, C.

*Centro de Física Teórica - Departamento de Física, Universidade de Coimbra, Coimbra, Portugal*

Publicação IF - 1384/99

# Droplet formation in cold asymmetric nuclear matter in the quark-meson-coupling model

G. Krein[1,2] * D.P. Menezes[3] † M. Nielsen[4] ‡ and C. Providência[5] §

*1. Department of Physics, University of Washington, Box 351560, Seattle - WA 98195-1560, USA*

*2. Instituto de Física Teórica, Universidade Estadual Paulista*

*R. Pamplona, 145 - 01405-900 São Paulo, SP, Brazil*

*3. Departamento de Física - CFM, Universidade Federal de Santa Catarina*

*Caixa Postal 476, 88.040-900 Florianópolis, SC, Brazil*

*4. Instituto de Física, Universidade de São Paulo*

*Caixa Postal 66318, 05315-970 São Paulo, SP, Brazil*

*5. Centro de Física Teórica - Departamento de Física, Universidade de Coimbra*

*3000 - Coimbra - Portugal*

## Abstract

The quark-meson-coupling model is used to study droplet formation from the liquid-gas phase transition in cold asymmetric nuclear matter. The critical density and proton fraction for the phase transition are determined in the mean field approximation. Droplet properties are calculated in the Thomas-Fermi approximation. The electromagnetic field is explicitly included and its effects on droplet properties are studied. The results are compared with the

*e-mail: gkrein@ift.unesp.br

†e-mail: fsc1dpm@fsc.ufsc.br

‡e-mail: mnielsen@if.usp.br

§e-mail: cp@teor.fis.uc.pt

ones obtained with the non-linear Walecka model.

PACS: 21.65.+f, 24.10.Jv, 25.75.-q, 12.39.-x KEYWORDS: Nuclear matter, liquid-gas phase transition, relativistic models, quark-meson coupling model

## I. INTRODUCTION

One of the most important problems in contemporary nuclear physics and astrophysics is the determination of the properties of nuclear matter as functions of density, temperature and the neutron-proton composition. In fact, neutron-star matter at densities between 0.03 $fm^{-3}$ and nuclear matter density consists of neutron-rich nuclei immersed in a gas of neutrons. In particular, understanding the transition crust-core in neutron stars is essential for explaining a number of properties of these stars [1]. To achieve this goal, one must study not only the ground and excited states of normal nuclei, but also nuclear states of high excitation and far from stability.

Recently, two of us studied droplet formation from the liquid-gas phase transition in cold [2] and hot [3] asymmetric nuclear matter in the context of the non-linear Walecka model (NLWM) [4]. In this paper we employ the quark-meson-coupling (QMC) model, originally proposed by Guichon [5]. In the QMC model, the mean scalar $\sigma$ and vector $\omega$ meson fields couple directly to the confined quarks inside the nucleon bags. The saturation of nuclear matter in this model is due to the density dependence of the effective $\sigma NN$ coupling, generated by the coupling of the mean $\sigma$ field to the quarks. As we shall show in this paper, this density dependence of the coupling has important consequences for the phase-transition and for the droplet radius and surface energy. While the QMC model shares many similarities with Walecka-type models [6], it however offers new opportunities for studying nuclear matter properties. Perhaps one of the most exciting ones is the possibility of using the same model to study nuclear phenomena in a large range of densities. With the QMC model, we have the opportunity to investigate the density regime where the quarks remain confined in the nucleon bags, but the stucture of the nucleons nevertheless changes, as became evident from the EMC effect [7]. We also expect to use the QMC model at much higher densities, where the nucleon bags start loosing their identity and the deconfinement transition starts taking place [8,9]. It is therefore important to explore the performance of the model in all such density regimes. Another good reason to use the QMC model in

the confined regime is that it might be of help to fix the low-energy constants of relativistic Lagrangians, where nucleon substructure is incorporated through a derivative expansion [10].

Since the original version of the model, there have been several ameliorations and extensions. These include the treatment of the nucleon center-of-mass motion [11,12], treatment of finite nuclei [13–15], change of the bag constant in medium [16], inclusion of finite temperature effects [17] and the treatment of Fock terms [18] and quark-exchange [19]. For a list of applications of the model to a variety of nuclear phenomena, see Ref. [20].

Within the framework of relativistic models, the liquid-gas phase transition in nuclear matter has been investigated at zero and finite temperatures for symmetric and asymmetric semi-infinite systems [21–24] and for finite systems [2,3]. The present study aims to study liquid-gas phase transition and droplet formation in a vapor system at zero temperature in the context of the QMC model and explore differences from the results of Refs. [2,3]. We include the Coulomb interaction and work in the Thomas-Fermi approximation. We determine the conditions for phase coexistence in a binary system by building the binodal section of the QMC model at zero temperature. As shown in Refs. [2,3], the optimal nuclear size of a droplet in a neutron gas is determined by a delicate balance between nuclear Coulomb and surface energies. The surface energy favors nuclei with a large number of nucleons $A$, while the nuclear Coulomb self-energy favors small nuclei. However, because of the density dependence of the effective $\sigma NN$ coupling in the QMC model, the critical pressure and proton fraction of the phase transition and the droplet properties turn out to be significantly different from the NLWM.

We also see that the presence of the outside neutron gas reduces the surface energy, since as the density of the system increases, the inside and outside matter become more and more alike.

The paper is organized as follows: in Sect. II we briefly summarize the QMC model for finite asymmetric systems including the couplings of the $\rho$ meson and the photon to the quarks. In Sect. III we discuss the Thomas-Fermi approximation and in Sect. IV we apply the model to asymmetric nuclear matter. Finally in Sects. V and VI we give our numerical

results and conclusions.

## II. THE QMC MODEL FOR FINITE ASYMMETRIC SYSTEMS

In a nucleus, the motion of the nucleon is relatively slow and the quarks are highly relativistic. The internal structure of the nucleon has therefore enough time to adjust to the external local meson fields, the motion of the nucleon can be treated as a point-like Dirac particle [13–15] with an effective mass $M_N^*$. The effective mass depends on the position only through the mean scalar field $\sigma$. To describe a finite system with different numbers of protons and neutrons, it is necessary to consider also the contribution of the $\rho$ meson. Besides, any realistic treatment of nuclear structure also requires that one introduces the Coulomb force. Therefore, a possible Lagrangian density for a static system is

$$\begin{aligned}\mathcal{L}_{QMC} = &\bar{\psi}[i\gamma\cdot\partial - M_N^*(\sigma(\mathbf{r})) - g_\omega\omega(\mathbf{r})\gamma_0 - g_\rho\frac{\tau_3^N}{2}b(\mathbf{r})\gamma_0 - \frac{e}{2}(1+\tau_3^N)A(\mathbf{r})\gamma_0]\psi \\ &- \frac{1}{2}[(\nabla\sigma(\mathbf{r}))^2 + m_\sigma^2\sigma(\mathbf{r})^2] + \frac{1}{2}[(\nabla\omega(\mathbf{r}))^2 + m_\omega^2\omega(\mathbf{r})^2] \\ &+ \frac{1}{2}[(\nabla b(\mathbf{r}))^2 + m_\rho^2 b(\mathbf{r})^2] + \frac{1}{2}(\nabla A(\mathbf{r}))^2\,, \end{aligned} \tag{1}$$

where $\psi(\mathbf{r})$, $\sigma(\mathbf{r})$, $\omega(\mathbf{r})$, $b(\mathbf{r})$ and $A(\mathbf{r})$ are respectively the nucleon, meson $\sigma$ and the mean values of the time component of $\omega$, $\rho$ and Coulomb fields in the nucleon rest frame; $\tau_3^N/2$ is the third component of the nucleon isospin operator; $m_\sigma$, $m_\omega$ and $m_\rho$ are respectively the masses of the $\sigma$, $\omega$ and $\rho$ fields; $g_\omega$ and $g_\rho$ are the $\omega - N$ and $\rho - N$ coupling constants, which are related to the corresponding quark coupling constants as $g_\omega = 3g_\omega^q$, $g_\rho = g_\rho^q$. Finally, $e$ is the electric charge.

The effective nucleon mass $M_N^*$ is calculated in the MIT bag model. Parameterizing the sum of the center-of-mass and gluonic fluctuation corrections in the familiar form $-z/R$, where $R^*$ is the in-medium bag radius, $M_N^*$ takes the form

$$M_N^* = \frac{3\Omega_q - z}{R^*} + \frac{4}{3}\pi B R^{*3}, \tag{2}$$

where $\Omega_q = \sqrt{x^{*2} + (R^* m_q^*)^2}$ is the kinetic energy of the quarks, $m_q^*(\mathbf{r}) = m_q - g_\sigma^q\sigma(\mathbf{r})$ is the

effective quark mass, $m_q$ is the bare quark mass, $g_\sigma^q$ is the quark-$\sigma$ coupling constant, and $x^*$ is the in-medium bag eigenvalue determined from the boundary condition

$$j_0(x^*) = \sqrt{\frac{\Omega_q - R^* m_q^*}{\Omega_q + R^* m_q^*}}\, j_1(x^*)\,. \tag{3}$$

The bag radius in obtained by minimizing $M_N^*$ with respect to $R^*$

$$\frac{\partial M_N^*}{\partial R^*} = 0\,, \tag{4}$$

and the bag constant $B$ and the parameter $z$ are fixed to reproduce the free-space nucleon mass ($M_N = 939$ MeV). In this work we use $m_q = 5$ MeV and fix the free bag radius at $R_B = 0.8$ fm. The results for $B$ and $z$ are: $B^{1/4} = 170.0$ MeV and $z = 3.295$. Results for $B$ and $z$ for other values of the bare quark mass and bag radius can be found in Ref. [15].

The variation of the Lagrangian, Eq. (1), results in the following equations for a spherically symmetric system

$$\frac{d^2}{dr^2}\sigma(r) + \frac{2}{r}\frac{d}{dr}\sigma(r) - m_\sigma^2\sigma(r) = -g_\sigma C(\sigma(r))\rho_s(r)\,, \tag{5}$$

$$\frac{d^2}{dr^2}\omega(r) + \frac{2}{r}\frac{d}{dr}\omega(r) - m_\omega^2\omega(r) = -g_\omega\rho_B(r)\,, \tag{6}$$

$$\frac{d^2}{dr^2}b(r) + \frac{2}{r}\frac{d}{dr}b(r) - m_\rho^2 b(r) = -\frac{g_\rho}{2}\rho_3(r)\,, \tag{7}$$

$$\frac{d^2}{dr^2}A(r) + \frac{2}{r}\frac{d}{dr}A(r) = -e\rho_p(r)\,, \tag{8}$$

where

$$g_\sigma C(\sigma) = -\frac{\partial M_N^*}{\partial\sigma} = 3g_\sigma^q S(\sigma)\,, \tag{9}$$

with

$$S(\sigma) = \frac{\Omega_q/2 + m_q^* R_B(\Omega_q - 1)}{\Omega_q(\Omega_q - 1) + m_q^* R_B/2}\,. \tag{10}$$

Note that the $\sigma - N$ coupling constant $g_\sigma$ is related to the quark-$\sigma$ coupling $g_\sigma^q$ through the relation

$$g_\sigma = 3\, g_\sigma^q\, S(0)\,, \tag{11}$$

and therefore

$$C(\sigma) = \frac{S(\sigma)}{S(0)}\,. \tag{12}$$

Also, in Eqs. (5) to (8), $\rho_s$ is the nucleon scalar density in the system with $A$ nucleons

$$\rho_s(r) = \langle A| \left[\bar{\psi}_p(r)\psi_p(r) + \bar{\psi}_n(r)\psi_n(r)\right] |A\rangle\,, \tag{13}$$

$\psi_p$ and $\psi_n$ are the proton and neutron spinors, respectively, and $\rho_B$ and $\rho_3$ are given in terms of the proton and neutron vector densities $\rho_p$ and $\rho_n$

$$\rho_B = \rho_p + \rho_n\,, \qquad \rho_3 = \rho_p - \rho_n, \tag{14}$$

with

$$\rho_p = \langle A|\psi_p^\dagger(r)\psi_p(r)|A\rangle, \qquad \rho_n = \langle A|\psi_n^\dagger(r)\psi_n(r)|A\rangle\,. \tag{15}$$

## III. THE THOMAS-FERMI APPROXIMATION

Since we want to compare results with Refs. [2,3], we employ the semi-classical Thomas-Fermi approximation, instead of solving the Dirac equation for the nucleons. This amounts to assuming that the mesonic fields vary slowly enough so that the baryons can be treated as moving in locally constant fields at each point of space. The basic quantity in the Thomas-Fermi approach is the phase-space distribution function for protons and neutrons

$$f_i(r,k) = \theta\left(k_{F_i}(r) - k\right), \quad i = p,n \tag{16}$$

where $k_{F_i}(r)$ is the local Fermi wave number for protons and neutrons. The total energy of the system is given by

$$\begin{aligned} E = 2\sum_{i=p,n}\int \frac{d^3k\,d^3r}{(2\pi)^3} f_i(r,k)h_i(r,k) + \frac{1}{2}\int d^3r\,\Big[(\nabla\sigma)^2 + m_\sigma^2\sigma^2 \\ - (\nabla\omega)^2 - m_\omega^2\omega^2 - (\nabla b)^2 - m_\rho^2 b^2 - (\nabla A)^2\Big]\,, \end{aligned} \tag{17}$$

where $h_i(r,k) = \sqrt{k^2 + {M_N^*}^2(\sigma(r))} + \nu_i(r)$, with

$$\nu_p(r) = g_\omega \omega(r) + \frac{g_\rho}{2} b(r) + eA(r) \ , \tag{18}$$

$$\nu_n(r) = g_\omega \omega(r) - \frac{g_\rho}{2} b(r) \ . \tag{19}$$

The thermodynamic potential is defined as

$$\Omega = E - \sum_{i=p,n} \mu_i N_i \ , \tag{20}$$

where $\mu_i$ is the chemical potential for particles of type $i$ and $N_p$ and $N_n$ are, respectively, the numbers of protons and neutrons

$$N_i = \int d^3r \, \rho_i(r), \quad i = p, n \ , \tag{21}$$

with the proton and neutron vector densities, $\rho_p$ and $\rho_n$ of Eq. (15), given explicitly by

$$\rho_i(r) = 2 \int \frac{d^3k}{(2\pi)^3} f_i(r,k) = \frac{1}{3\pi^2} k_{F_i}^3(r) \, . \tag{22}$$

Minimizing the thermodynamic potential $\Omega$ with respect to the local Fermi momentum, the following expressions for the proton and neutron chemical potentials are obtained

$$\mu_p = \sqrt{k_{F_p}^2 + {M_N^*}^2} + g_\omega \omega + \frac{g_\rho}{2} b + eA \ , \tag{23}$$

$$\mu_n = \sqrt{k_{F_n}^2 + {M_N^*}^2} + g_\omega \omega - \frac{g_\rho}{2} b \ , \tag{24}$$

which can be used to find $k_{F_i}(M_N^*, \omega, b, A, \mu_i; r)$.

The fields that minimize $\Omega$ satisfy Eqs. (5) to (8), where the scalar density of Eq.( 13) is given explicitly by

$$\rho_s(r) = 2 \sum_{i=p,n} \int \frac{d^3k}{(2\pi)^3} \frac{M_N^*(\sigma(r))}{\sqrt{k^2 + {M_N^*}^2(\sigma(r))}} f_i(r,k) \, . \tag{25}$$

## IV. LIQUID-GAS PHASE TRANSITION IN ASYMMETRIC NUCLEAR MATTER

Phase transitions in binary systems are more complex than in one-component systems because two kinds of instabilities can occur. We have therefore two stability conditions. We have the condition for mechanical stability, which requires

$$\left(\frac{\partial P}{\partial \rho_B}\right)_{Y_p} \geq 0\,, \tag{26}$$

where $P$ is the pressure and $Y_p = \rho_p/\rho_B$ is the proton fraction. We have also the condition for diffusive stability, which implies the inequalities

$$\left(\frac{\partial \mu_p}{\partial Y_p}\right)_P \geq 0 \quad \text{and} \quad \left(\frac{\partial \mu_n}{\partial Y_p}\right)_P \leq 0\,. \tag{27}$$

These reflect the fact that in a stable system, energy is required to increase the proton concentration while the pressure is kept constant.

In the mean field approximation for infinite nuclear matter, the meson fields are replaced by their expectation values and Eqs. (5) to (8) become (omitting the electromagnetic field)

$$\overline{\sigma} = \frac{g_\sigma}{m_\sigma^2} C(\overline{\sigma}) \rho_s\,, \tag{28}$$

$$\overline{\omega} = \frac{g_\omega}{m_\omega^2} \rho_B\,, \tag{29}$$

$$\overline{b} = \frac{g_\rho}{2m_\rho^2} \rho_3\,, \tag{30}$$

where the sources of the fields are constants and can be related to the nucleon Fermi momentum $k_{F_i}$ through

$$\rho_s = 2 \sum_{i=p,n} \int \frac{d^3k}{(2\pi)^3} \theta(k_{F_i} - k) \frac{M_N^*(\overline{\sigma})}{\sqrt{M_N^{*\,2}(\overline{\sigma}) + k^2}}\,, \tag{31}$$

$$\rho_i = 2 \int \frac{d^3k}{(2\pi)^3} \theta(k_{F_i} - k) = \frac{1}{3\pi^2} k_{F_i}^3\,. \tag{32}$$

Under this approximation, the energy density and pressure are given by

$$\mathcal{E} = 2 \sum_{i=p,n} \int \frac{d^3k}{(2\pi)^3} \sqrt{k^2 + M_N^{*\,2}(\overline{\sigma})}\; \theta(k_{F_i} - k) + \frac{g_\omega^2 \rho_B^2}{2m_\omega^2} + \frac{g_\rho^2 \rho_3^2}{8m_\rho^2} + \frac{m_\sigma^2}{2} \overline{\sigma}^2\,, \tag{33}$$

$$P = \frac{2}{3} \sum_{i=p,n} \int \frac{d^3k}{(2\pi)^3} \frac{k^2\, \theta(k_{F_i} - k)}{\sqrt{k^2 + M_N^{*\,2}(\overline{\sigma})}} + \frac{g_\omega^2 \rho_B^2}{2m_\omega^2} + \frac{g_\rho^2 \rho_3^2}{8m_\rho^2} - \frac{m_\sigma^2}{2} \overline{\sigma}^2\,. \tag{34}$$

There are six parameters to be determined: $g_\sigma$, $g_\omega$, $g_\rho$, $m_\sigma$, $m_\omega$ and $m_\rho$. We take the experimental values of $m_\omega = 783$ MeV and $m_\rho = 770$ MeV, and the other parameters are taken from Ref. [15]: $g_\sigma^2/4\pi = 3.12$, $g_\omega^2/4\pi = 5.31$, $g_\rho^2/4\pi = 6.93$ and $m_\sigma = 418$ MeV.

The two-phase liquid-gas coexistence is governed by the Gibbs condition

$$\mu_i(\rho_p, \rho_n, M_N^*) = \mu_i(\rho_p', \rho_n', M_N^{*\prime}), \quad i = p, n \tag{35}$$

$$P(\rho_p, \rho_n, M_N^*) = P(\rho_p', \rho_n', M_N^{*\prime}) \, . \tag{36}$$

We have made use of the geometrical construction [25,26] in order to obtain the chemical potentials in the two coexisting phases for each pressure of interest. In Fig. 1 we plot $\mu_p$ and $\mu_n$ as a function of the proton fraction for $P = 0.1$ MeV/fm$^3$ (solid line). For comparison, we also show in this figure the results obtained with the Walecka model [6] (dotted line) and with the non-linear Walecka model [4], discussed in Refs. [2,3] (NLWM) (dashed line).

In order to obtain the binodal section, which gives the pairs of points under the same pressure for different proton fractions obtained using the geometrical construction, we have used the condition of the diffusive stability, Eq.(27), and solved simultaneously Eqs. (35) and (36), together with

$$\overline{\sigma} = \frac{g_\sigma}{m_\sigma^2} C(\overline{\sigma}) \rho_s(\rho_p, \rho_n, M_N^*) \, , \tag{37}$$

$$\overline{\sigma}' = \frac{g_\sigma}{m_\sigma^2} C(\overline{\sigma}') \rho_s(\rho_p', \rho_n', M_N^{*\prime}) \, . \tag{38}$$

The binodal section is shown in Fig. 2 for the QMC model (solid line). It is divided into two branches by the critical point (CP). One branch describes the system in a high-density (liquid) phase, while the other branch describes the low-density (gas) phase. The liquid (gas) phase appears at the right (left) of CP.

For finite temperatures, $T \neq 0$, the gas phase is also characterized by $Y_p \neq 0$ for all values of the pressure. However, for $T = 0$ and for $P \lesssim 0.43$ MeV fm$^{-3}$, the gas phase always has $Y_p = 0$. For the sake of completeness, we also show in Fig. 2 the binodal sections for the NLWM discussed in refs. [2,3] (dashed line). We see that the QMC has a CP with higher values of $P$ and $Y_p$, but that in the liquid phase it is mainly characterized, for a given pressure $P$, by smaller values of $Y_p$ than the NLWM.

## V. NUMERICAL RESULTS FOR FINITE SYSTEMS

The solution for the infinite system gives us the initial and boundary conditions for the program which integrates the set of coupled non-linear differential equations (5) to (8) in the Thomas-Fermi approximation. In this work the numerical calculation was carried out with the iteration procedure described in Ref. [2], which uses also as input the size of the mesh, $R_{mesh}$. The size of the mesh determines the size of the droplet and, consequently, the chemical potentials and the number of particles in the droplet. Hence, the number of particles and the proton fraction within the droplet are output of the program and not fixed from the start. The same is true for the liquid and gas proton fractions. In order to obtain a certain number of particles inside the droplet, we vary $R_{mesh}$ for a given initial condition until the desired number is obtained as output. Therefore, by fixing the number of the particles in the droplet we can study the behavior of some of its properties, such as the surface energy, neutron thickness, proton radius, etc., as a function of the initial (liquid) proton fraction. For more details about this numerical procedure we refer the reader to Refs. [2,3].

In order to understand the differences between the QMC and NLWM in the Thomas-Fermi approximation, we have calculated the proton density of a droplet with total particle number $A = 40$ and proton fraction $N_p/A = 0.5$. The results are shown in Fig. 3. The solid and dashed lines show the results for QMC and NLWM, respectively. It is clear from this figure that the QMC result shows higher central density and smaller proton radius. This feature is present in all solutions we have obtained. This can be explained by the different values of the incompressibility, $K$, of the models. The higher the value of $K$, more similar to a theta function the density distribution becomes. The value of $K$ for the two models analyzed here are $K_{QMC} \simeq 280$ MeV, $K_{NLWM} \simeq 210$ MeV. Of course the result for the Walecka model has a smaller surface thickness than the models studied here since $K_{QHD} \simeq 550$ MeV.

The droplet surface energy per unit area in the small thickness approximation is given

by [2,3,27]

$$\mathcal{E}_{surf} = \int_0^\infty dr \left[ \left(\frac{d\sigma}{dr}\right)^2 - \left(\frac{d\omega}{dr}\right)^2 - \left(\frac{db}{dr}\right)^2 \right]. \tag{39}$$

In Ref. [2] the results obtained from this expression for the density surface energy were parametrized and compared with the liquid drop model results. The conclusion was that, albeit approximate, Eq. (39) provides a very good estimate of the density surface energy.

The proton and neutron radii in spherical geometry, $R_i$ $(i = p, n)$, are defined as

$$\int_0^{R'} \rho_p(r) r^2 dr = \frac{1}{3}\left[\rho_{p,g} R_p^3 + \rho_{p,l}(R'^3 - R_p^3)\right], \tag{40}$$

and

$$\int_0^{R'} \rho_n(r) r^2 dr = \frac{1}{3}\left[\rho_{n,g} R_n^3 + \rho_{n,l}(R'^3 - R_n^3)\right], \tag{41}$$

where $\rho_{i,l}$ and $\rho_{i,g}$ refers to the liquid and gas density respectively; $R'$ is the value of $r$ such that $|f(r) - f_g| < 10^{-8}$, with $f$ being either a meson field or the baryonic density at $r$, and $f_g$ the corresponding gas value. This means that $R'$ is the value of $r$ for which the fields and density reach their asymptotic gas values.

Another important quantity is the thickness of the region at the surface with extra neutrons known as *neutron skin*. The *neutron skin thickness* is defined as [24]

$$\Theta = R_n - R_p. \tag{42}$$

In Fig. 4 we show the surface energy density for a droplet with total particle number $A = N_p + N_n = 20$, with (dashed line) and without (solid line) the electromagnetic field. For comparison we also show in this figure the result (without the Coulomb field) for the NLWM (dotted line). As we can see, the differences resulting from different models are much larger than the differences due to the inclusion of the electromagnetic field. The density surface energy increases with the initial proton fraction. In fact for small proton fraction, the matter inside the droplet becomes more and more neutron rich and, at the same time, the density difference between the matter inside and outside the droplet becomes smaller. Were the

matter inside and outside the same, of course there would be no surface energy. This effect was already observed in earlier studies of neutron star matter [28]. Comparing the QMC and NLWM, we see that the density surface energy in the latter is smaller, possibly due to the higher incompressibility of the former. This could have as consequence a thinner crust-bulk transition in the neutron star described by the QMC model. We also see that the Coulomb field, a long range force, does not change much the density surface energy of the droplet, as expected.

In Fig. 5 we show the density surface energy for droplets with $A = 20$ (dashed line) and $A = 40$ (solid line), both with the inclusion of the electromagnetic field, as a function of the initial proton fraction. We see that the density surface energy increases with the total number of particles in the droplet. This is because the systems we studied, with $A = 20$, are not big enough and, therefore, $\mathcal{E}_{surf}$ depends on $R$, the size of the droplet. In general $\mathcal{E}_{surf}$ is identified with the surface energy associated with an infinite plane surface with a finite thickness, with the matter on one side being in the liquid phase and on the other in the gas phase. We have checked that the density surface energy *does not* change appreciably in going from systems with $A = 40$ to $A = 60$.

It should be stressed that when the Coulomb field is present the solution $Y_p(r = 0) = 0.5$ does not exist in our formalism, since the Coulomb field favors an increase of the neutron fraction.

In Fig. 6 we show the proton radius as a function of the initial proton fraction for the QMC model with (dashed line) and without (solid line) the contribution of the Coulomb field, and for the NLWM without the Coulomb field (dotted line) for a droplet with $A = 20$. As the equation of state of the NLWM is softer than the QMC, the proton radius is larger in the former. It is interesting to notice that for $Y_p(0)$ in the interval $(0.4 - 0.45)$, $R_p$ has a minimum. This is due to a competition between the repulsive Coulomb force between protons and the attractive force between nucleons. Of course the inclusion of the Coulomb field increases the proton radius (due to repulsion).

The fact that for small values of the liquid proton fraction, $R_p$ is smaller when the

Coulomb field is included is because for these droplets the total proton fraction in the droplet is in fact smaller than the total proton fraction in the droplet without the Coulomb field, as can be seen in Fig. 7 where we plot the total proton fraction in the droplet ($Y_{tot} = N_p/A$) as a function of the initial proton fraction in the system.

Finally, in Fig. 8 we show the neutron skin thickness as a function of the initial proton fraction for a droplet with $A = 20$ for the QMC model with (dashed line) and without (solid line) the contribution of the Coulomb field, and for the NLWM without the Coulomb field (dotted line). We see that the behavior is very similar in both models, the neutron skin being thicker in the latter because of its softer surface. We also see that the contribution of the Coulomb field decreases the neutron skin thickness, since the proton radius $R_p$ increases.

It is worth pointing out that no results were shown for very small proton fractions because, for the desired total number of particles (20 and 40) we did not abtain convergence for the coupled differential equations.

## VI. CONCLUSIONS

In this work we have studied, within the framework of the QMC model, the surface properties of droplets which arise from the liquid-gas phase transition under conditions predetermined by the binodal section. The droplets are described using the Thomas-Fermi approximation. The results are then compared with the NLWM.

Some of the consequences of the electromagnetic field in the droplet formation within the QMC model, for a fixed number of particles, is to increase the surface energy and to decrease the neutron skin thickness, except for very small proton fractions or for almost symmetric nuclear matter. However, the effect of the electromagnetic field is very tiny in surface properties and the differences resulting from the use of different models are by far more important.

We think that the different incompressibilities of the models are, probably, the main reason for the differences in the surface properties. Since the QMC model has a harder

equation of state, it has a higher density surface energy, smaller proton radius and smaller neutron skin thickness as compared with the NLWM.

We also note that while our numerical results depend on the particular model chosen (namely, the QMC or NLW models), some qualitative features such as the increase of the surface energy density, the increase of the total proton fraction and the decrease of the neutron skin thickness with the initial proton fraction in the droplet, apply to both models.

The inclusion of finite temperature effects in droplet formation within the QMC model is, of course, a natural extension of our calculation and work in this direction is under consideration.

## ACKNOWLEDGMENTS

This work was supported in part by the University of Washington (USA), CNPq and FAPESP (Brazil) and FCT (Portugal). M.N. would like to thank the Centro de Física Teórica da Universidade de Coimbra for its hospitality and financial support during her stay in Portugal. The authors also acknowledge useful discussions with Dr. C.A. Bertulani and Dr. M.B. Pinto.

# REFERENCES


[1] C.J. Pethick, D.G. Ravenhall, C.P. Lorenz, Nucl. Phys. A 584 (1995) 675.

[2] D.P. Menezes and C. Providência, Nucl. Phys.A 650 (1999) 283.

[3] D.P. Menezes and C. Providência, Phys. Rev. C 60 (1999) 024313.

[4] J. Boguta and A. R. Bodmer, Nucl. Phys. A 292 (1977) 413; A.R. Bodmer and C.E. Price, Nucl. Phys. A 505 (1989) 123; P.-G. Reinhard, M. Rufa, J. Maruhn, W. Greiner and J. Friedrich, Z. Phys. A323 (1986) 13.

[5] P.A.M. Guichon, Phys. Lett. B 200 (1988) 235.

[6] B.D. Serot and J.D. Walecka, Adv. Nucl. Phys. 16 (1986) 1.

[7] M. Arneodo, Phys. Rep. 240 (1994) 301; D.F. Geesaman, K. Saito and A.W. Thomas, Annu. Rev. Nucl. Part. Sci. 45 (1995) 337 .

[8] I. Zakout and H. R. Jaqaman, Phys.Rev. C 59 (1999) 962.

[9] S. Pal, M. Hanauske, I. Zakout, H. Stöcker and W. Greiner, Phys. Rev. C 60 (1999) 015802.

[10] R.J. Furnstahl, B.D. Serot and H.-B. Tang, Nucl. Phys. A 598 (1996) 539; 615 (1997) 441; 618 (1997) 446.

[11] S. Fleck, W. Bentz, K. Shimizu and K. Yazaki, Nucl. Phys. A 510 (1990) 731.

[12] K. Saito and A.W. Thomas, Phys. Lett. B 327 (1994) 9 .

[13] P.A.M. Guichon, K. Saito, E. Rodionov and A.W. Thomas, Nucl. Phys. A 601 (1996) 349.

[14] P.G. Blunden and G.A. Miller, Phys. Rev. C 54 (1996) 359.

[15] K. Saito, K. Tsushima and A.W. Thomas, Nucl. Phys. A 609 (1996) 339.

[16] X. Jin and B.K. Jennings, Phys. Lett. B 374 (1996) 13; Phys. Rev. C 54 (1996) 1427; H. Müller and B.K. Jennings, Nucl. Phys. A 640 (1988) 55.

[17] P. K. Panda, A. Mishra, J. M. Eisenberg and W. Greiner, Phys.Rev. C 56 (1997) 3134; I. Zakout and H. R. Jaqaman, Phys.Rev. C 59 (1999) 968.

[18] G. Krein, A.W. Thomas and K. Tsushima, Nucl. Phys. A 610 (1999) 313.

[19] M.E. Bracco, G. Krein and M. Nielsen, Phys .Lett. B 432 (1998) 258.

[20] A.W. Thomas, Nucl. Phys. A 629 (1998) 20.

[21] H. Reinhardt and H. Schulz, Nucl. Phys. A432 (1985) 630.

[22] H. Müller and R.M. Dreizler, Nucl. Phys. A 563 (1993) 649.

[23] D. Von Eiff, J. M. Pearson, W. Stocker and M. K.Weigel, Phys. Lett. B 324 (1994) 279.

[24] M. Centelles, M. Del Estal and X. Viñas, Nucl. Phys. A 635 (1998) 193.

[25] M. Barranco and J.R. Buchler, Phys. Rev. C 22 (1980) 1729.

[26] H. Müller and B.D. Serot, Phys. Rev. C 52 (1995) 2072.

[27] M. Nielsen and J. Providência, J. Phys. G 16 (1990) 649.

[28] G. Baym, H.A. Bethe and C.J. Pethick, Nucl. Phys. A 175 (1971) 225.

[29] C. Speicher, E. Engel and R.M. Dreizler, Nucl. Phys. A 562 (1993) 569.

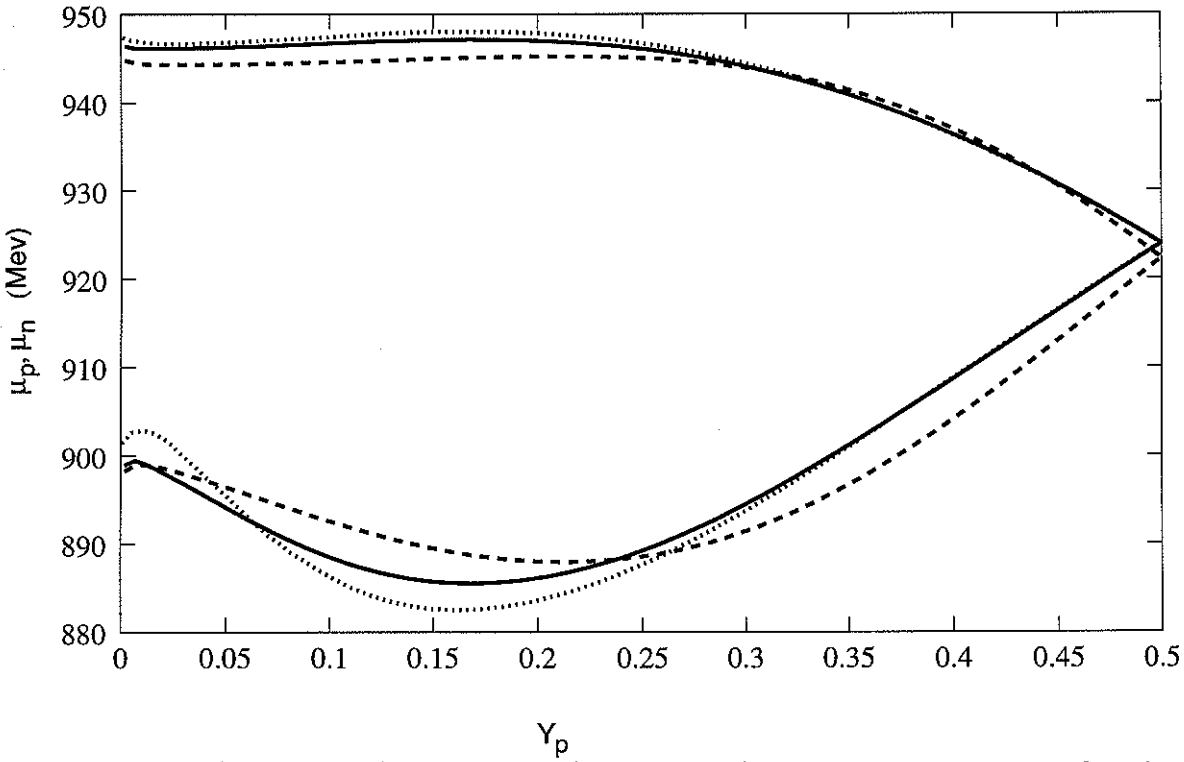


FIG. 1. Proton (lower curves) and neutron (upper curves) chemical potentials as a function of the proton fraction for $P = 0.1$ MeV/fm$^3$ for the QMC model (solid lines), for the Walecka model (dotted lines), and for the NLWM (dashed lines).

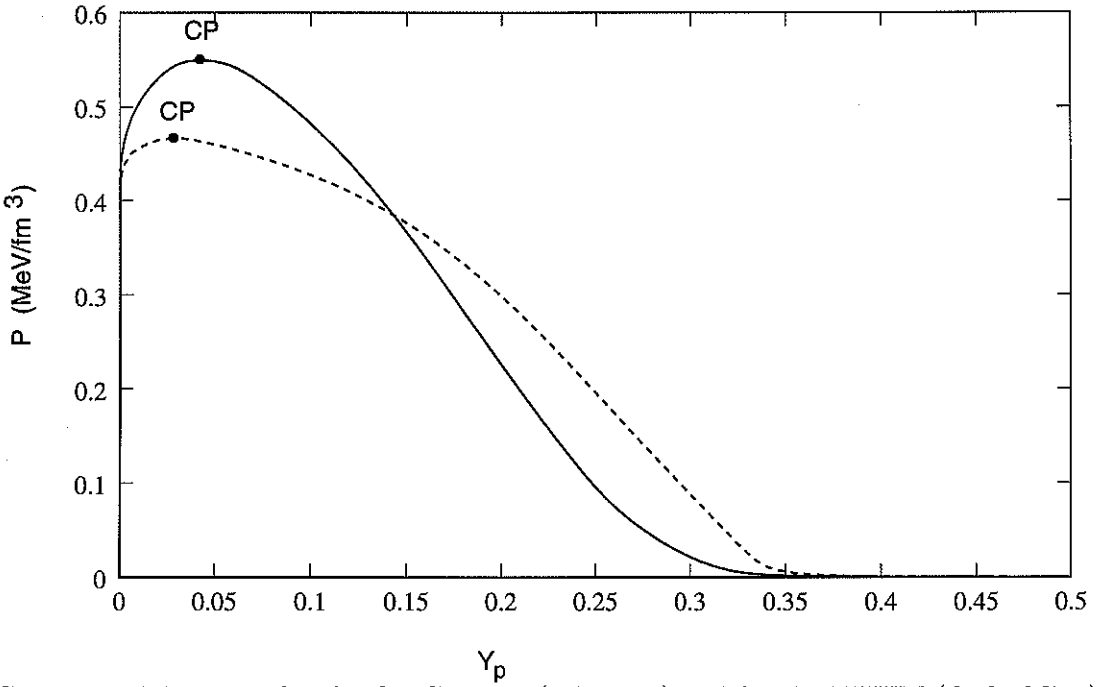


FIG. 2. Binodal section for the QMC model (solid line) and for the NLWM (dashed line). The critical point (CP) is indicated; the liquid (gas) phase is to the right (left) of CP.

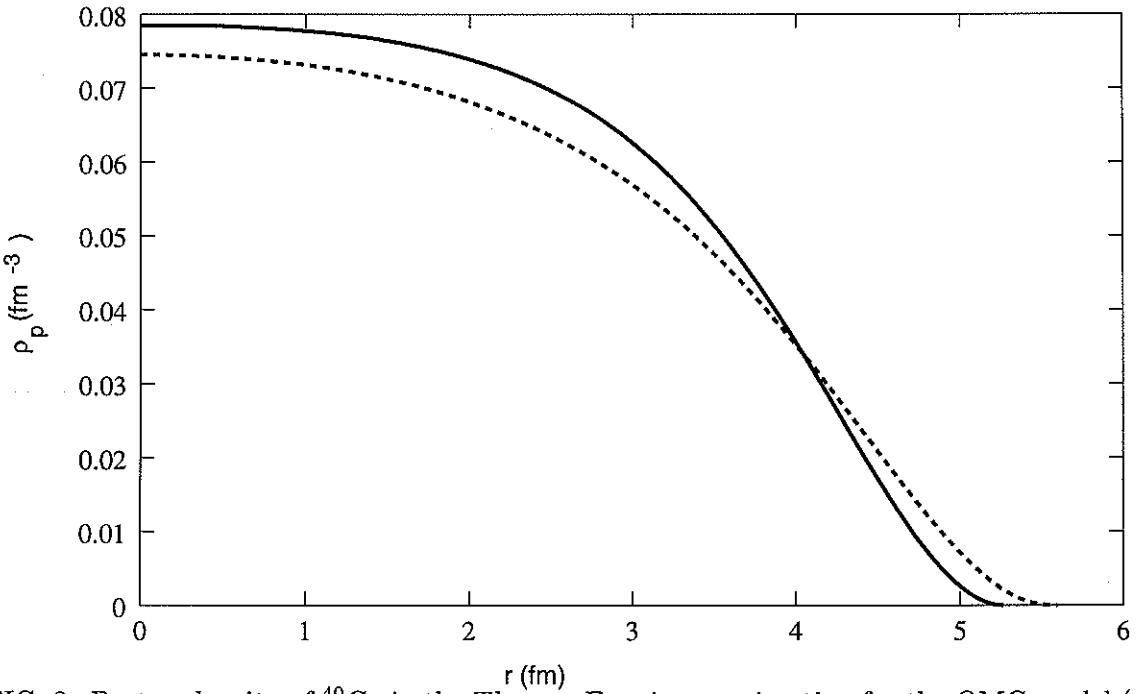


FIG. 3. Proton density of $^{40}$Ca in the Thomas-Fermi approximation for the QMC model (solid line) and for the NLWM (dashed line).

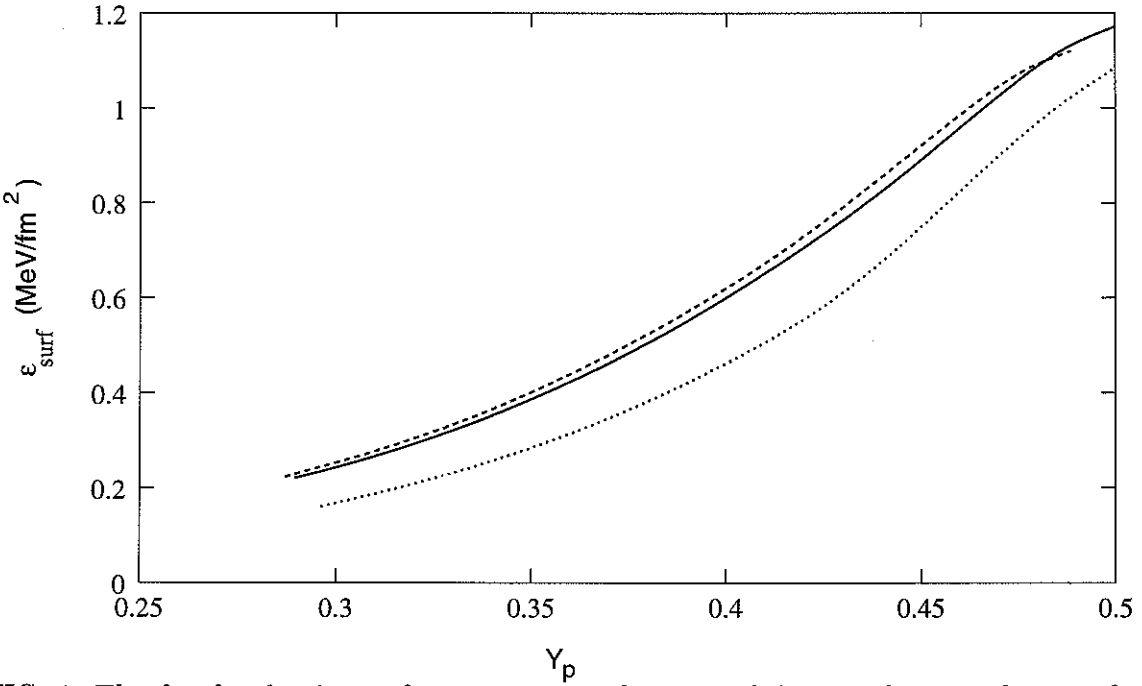


FIG. 4. The droplet density surface energy as a function of the initial proton fraction for the QMC model with (dashed line) and without (solid line) the electromagnetic field, and for the NLWM without the electromagnetic field (dotted line). Results for a droplet with a total of 20 particles.

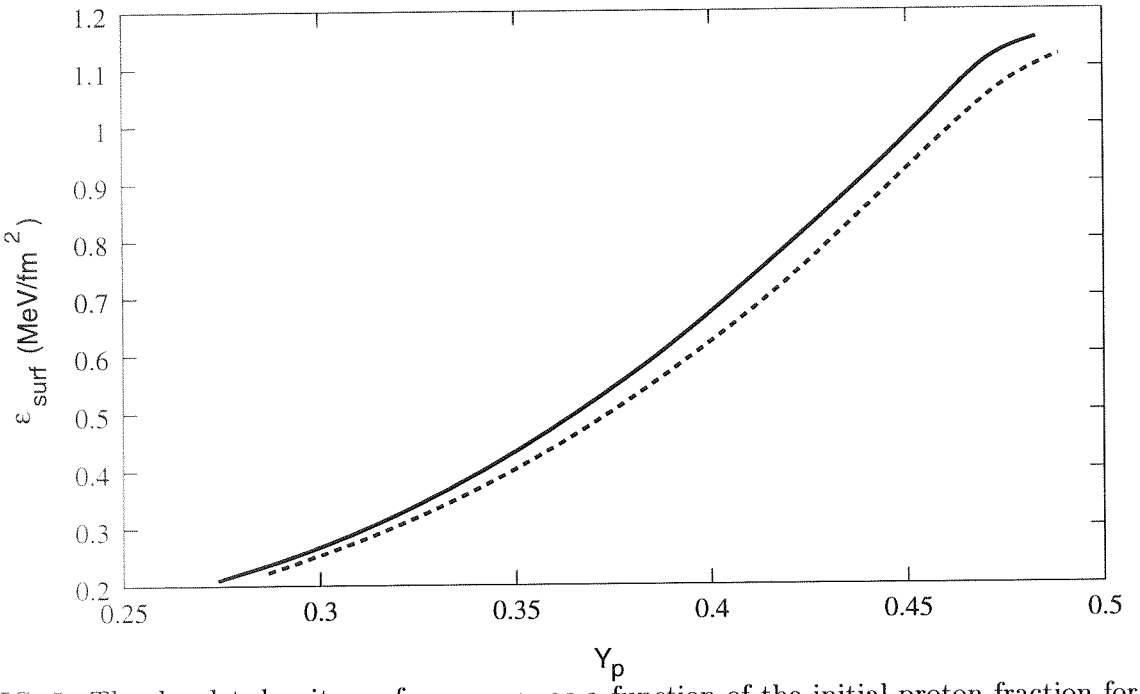


FIG. 5. The droplet density surface energy as a function of the initial proton fraction for the QMC model with the electromagnetic field for a droplet with a total of 40 (solid line) and 20 (dashed line) particles.

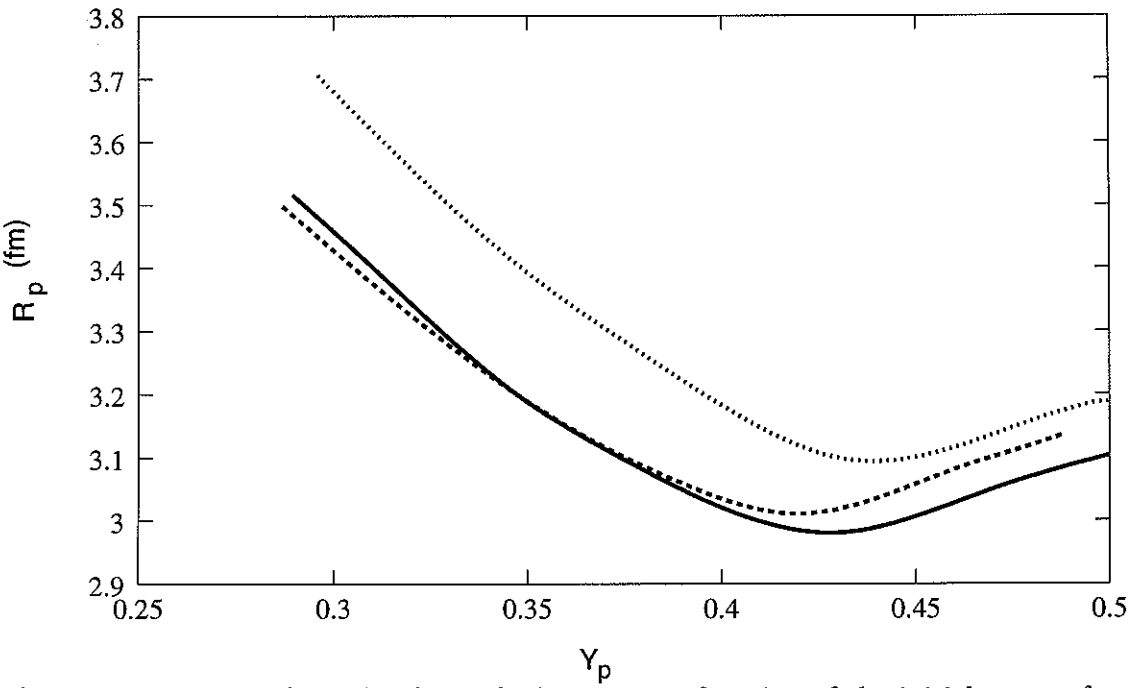


FIG. 6. Proton radius for a droplet with $A = 20$ as a function of the initial proton fraction. The meaning of the lines is the same as in Fig. 4.

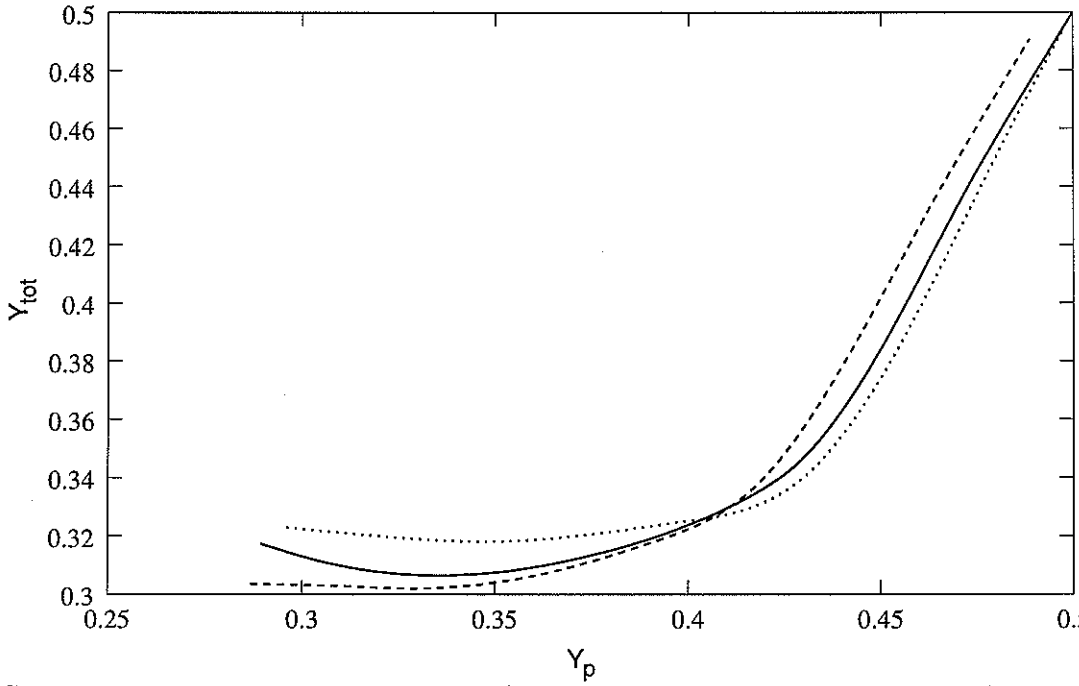


FIG. 7. Total proton fraction $Y_{tot} = N_p/A$ in the droplet with $A = 20$ as a function of the initial proton fraction. The meaning of the lines is the same as in Fig. 4.